Geochemistry Geophysics Geosystems G3

Article
Volume 11, Number 12
31 December 2010
Q12015, doi:10.1029/2010GC003264
ISSN: 1525-2027

Published by AGU and the Geochemical Society

A seismic swarm and regional hydrothermal and hydrologic perturbations: The northern Endeavour segment, February 2005

Emilie E. E. Hooft
Department of Geological Sciences, University of Oregon, Eugene, Oregon 97403, USA (emilie@uoregon.edu)

Hemalinee Patel
British Petroleum, 501 Westlake Park Boulevard, Houston, Texas 77079, USA

William Wilcock
School of Oceanography, University of Washington, Seattle, Washington 98195, USA

Keir Becker
Rosenstiel School of Marine and Atmospheric Sciences, University of Miami, Miami, Florida 33149, USA

David Butterfield
Pacific Marine Environmental Laboratory, NOAA, Seattle, Washington 98115, USA

Earl Davis
Pacific Geoscience Center, Geological Survey of Canada, Sidney, British Columbia V8L 4B2, Canada

Robert Dziak
Pacific Marine Environmental Laboratory, NOAA, Newport, Oregon 97365, USA

Katherine Inderbitzen
Rosenstiel School of Marine and Atmospheric Sciences, University of Miami, Miami, Florida 33149, USA

Marvin Lilley
School of Oceanography, University of Washington, Seattle, Washington 98195, USA

Paul McGill
Monterey Bay Aquarium Research Institute, Moss Landing, California 95039, USA

Douglas Toomey
Department of Geological Sciences, University of Oregon, Eugene, Oregon 97403, USA

Debra Stakes
Division of Physical Sciences, Cuesta College, San Luis Obispo, California 93403, USA

[1] The February 2005 swarm at the overlapping spreading center (OSC) on the northern end of the Endeavour segment is the first swarm on the Juan de Fuca Ridge recorded on a local seafloor seismic network. The swarm included several larger earthquakes and caused triggered seismicity and a hydrothermal response in the Endeavour vent fields as well as regional-scale hydrologic pressure perturbations. The spatial and temporal pattern of over 6000 earthquakes recorded during this seismic sequence is complex. Small-magnitude events dominate, and seismicity rates wax and wane, indicating a magmatic process. The main swarm initiates at the northern end of the Endeavour ridge. However, most of the moment release, including six strike-slip events, occurs in the southwest Endeavour Valley, where the swarm epicenters generally migrate south. The main swarm is contemporaneous with a hydrologic pressure response at four sealed seafloor boreholes, ~25–105 km away. We infer that the seismic sequence is driven by a largely aseismic magma intrusion at the northern Endeavour axis. Resulting stress changes trigger slip on tectonic faults and possibly dike propagation at the opposing limb of the Endeavour OSC in the southwest Endeavour Valley, consistent with the eventual decapitation of the Endeavour by the West Valley segment. Furthermore, 2.5 days after the start of the main swarm, seismicity is triggered beneath the Endeavour vent fields, and temperature increases at a diffuse vent in the Mothra field. We infer that this delayed response is due to a hydrologic pressure pulse that diffuses away from the main magma intrusion.

Components: 12,700 words, 11 figures, 2 tables.

Keywords: earthquake swarm; hydrothermal response; hydrologic response; magma intrusion; overlapping spreading center; Endeavour ridge.

Index Terms: 3035 Marine Geology and Geophysics: Midocean ridge processes; 3025 Marine Geology and Geophysics: Marine seismics (0935, 7294); 7280 Seismology: Volcano seismology (8419).

Received 18 June 2010; **Revised** 12 October 2010; **Accepted** 4 November 2010; **Published** 31 December 2010.

Hooft, E. E. E., et al. (2010), A seismic swarm and regional hydrothermal and hydrologic perturbations: The northern Endeavour segment, February 2005, *Geochem. Geophys. Geosyst.*, *11*, Q12015, doi:10.1029/2010GC003264.

1. Introduction

[2] Stress changes in the shallow, brittle crust that are related to magmatic intrusions, tectonic faulting or hydrothermal cooling are the cause of most seismic swarms at mid-ocean ridges and result in abrupt increases in the number and rate of earthquakes. As such, the distribution of earthquakes in space and time is a primary source of information about the nature of subsurface geological processes [*Tolstoy*, 2008]. The stress changes during these episodes may impact fluid flow and the biological communities that rely on the resulting chemical and thermal exchange. Deciphering the relative role of magmatism, tectonism and fluid flow during such episodes is essential to understanding the dynamic, interlinked environment at mid-ocean ridges.

[3] Tectonic swarms typically consist of a series of earthquakes following a main shock fault rupture. The seismicity rate of tectonic swarms decreases exponentially with time according to the modified Omori's law [*Utsu*, 1961]. The magnitude distribution of earthquakes is described by the Gutenberg-Richter relationship, where the slope of the log of cumulative frequency versus magnitude distribution, or *b* value, describes the relative proportion of small and large magnitude events [*Gutenberg and Richter*, 1944]. While globally the *b* value is approximately one [e.g., *Frohlich and Davis*, 1993], *b* values vary at both local and regional scales [e.g., *Wiemer and Wyss*, 2002]. Elevated *b* values are related to low-stress conditions [e.g., *Amitrano*, 2003; *Scholz*, 1968], high pore pressure [e.g., *Wiemer et al.*, 1998], or greater heterogeneity and variability in the distribution of fractures [e.g., *Wyss et al.*, 2004]. For tectonic aftershock swarms the *b* value is often close to 1, similar to the global average, indicating that most of the tectonic stress is relieved by the larger earthquakes.

[4] In contrast, for seismic swarms that accompany a magmatic intrusion, the rate and epicentral distribution of seismic events varies notably over the course of the intrusion. For instance, when a dike intrudes the oceanic crust and propagates laterally, earthquakes are generated by rock breaking around the dike tip and the epicenters follow the dike propagation [e.g., *Dziak and Fox*, 1999; *Dziak et al.*, 1995; *Fox and Dziak*, 1998]. In this case there are

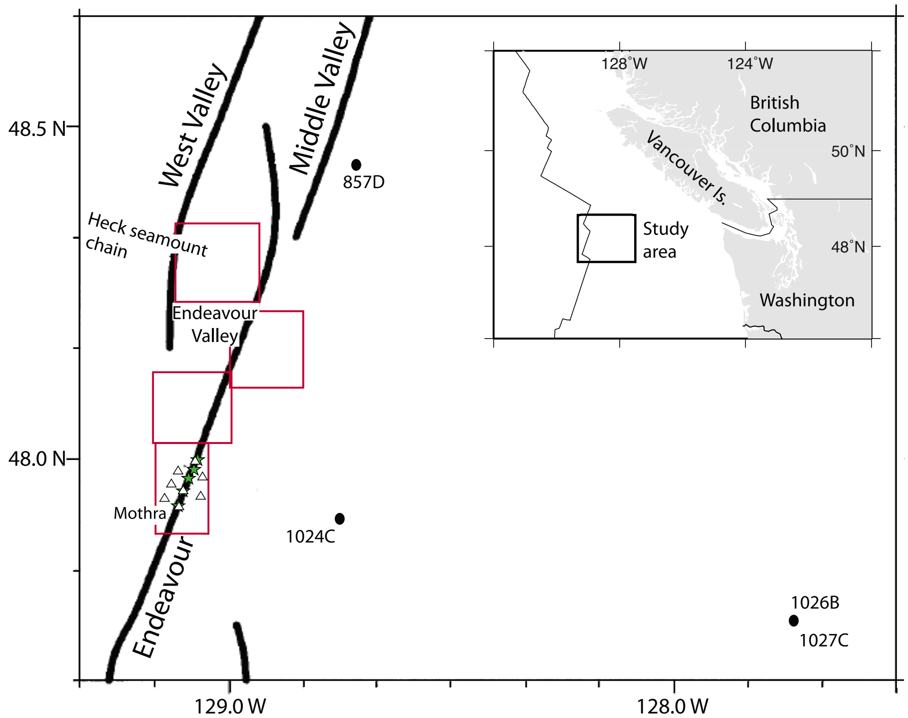

Figure 1. Regional overview showing the axes of the active Endeavour and West Valley ridge segments and the abandoned Middle Valley segment in dark lines. The Endeavour Valley is located in the overlapping spreading center (OSC) between the West Valley and Endeavour segments. The Heck seamount chain lies to the east and intersects the northern portion of the OSC. The sealed seafloor boreholes monitored for formation pressure (IODP CORKs) are labeled black circles. The Keck seismometers (white triangles) and Endeavour vent fields (green stars) are shown with the Mothra diffuse vent field labeled. The four regions within the swarm are outlined with red rectangles.

relatively more small magnitude events and b values are typically greater than 1 (up to 3) [*Wiemer and Wyss*, 2002]. In concert with dike intrusions, pre-existing faults that are near critical stress may fail as the dike modifies the local stress field [*Rubin and Gillard*, 1998]. Any earthquakes triggered by a magmatic intrusion will be followed by their own aftershock sequences.

[5] Stress and strain changes resulting from seismic deformation affect fluid flow patterns in the crust and can modify the physical, chemical and biological processes at the ridge crest. At mid-ocean ridges such perturbations of hydrothermal systems have been associated with both large regional earthquakes [*Dziak et al.*, 2003; *Johnson et al.*, 2000] and local tectonic microearthquake swarms [*Sohn et al.*, 1999]. In continental geothermal systems triggered earthquakes are commonly observed in response to stress changes due to regional events as well as the passage of seismic waves from large distant earthquakes [*Brodsky and Prejean*, 2005; *Brodsky et al.*, 2000; *Hill et al.*, 1993; *Kilb et al.*, 2000]. At mid-ocean ridges we anticipate triggered seismicity because the faults in the extending brittle crust are close to failure and because stresses may be amplified in the brittle zones that surround magma bodies and hot ductile regions. Local earthquake swarms may perturb hydrothermal systems either by opening a new passage way to a high-temperature region in the reaction zone, thereby increasing the flow rates and/or temperatures, or by increasing the permeability at a choke point within the existing upflow path, thus allowing the system to depressurize [*Wilcock*, 2004].

[6] In this paper we use data from a local seismic network to describe a complex seismic sequence at the northern end of the Endeavour segment of the Juan de Fuca ridge that occurred in late February 2005, as well as the associated hydrothermal and hydrologic perturbations (Figure 1). The spatial and temporal patterns of epicentral locations and magnitudes for over 6000 earthquakes together with temperature perturbations at hydrothermal vent fields and contemporaneous pressure changes in

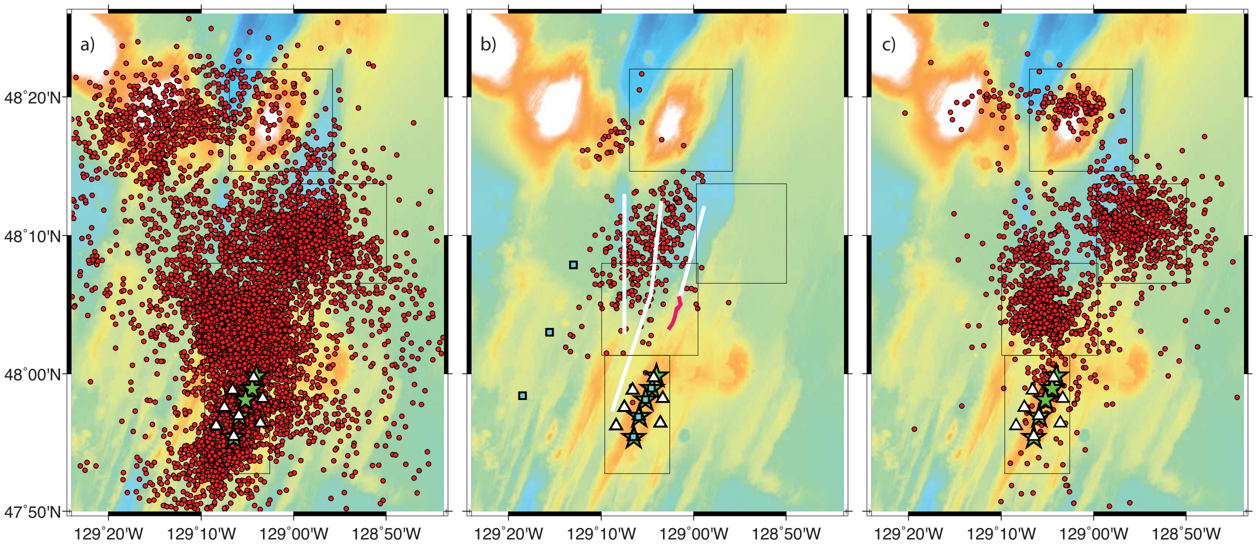

Figure 2. (a) Keck network seismicity August 2003 to August 2004. Map of the seismicity for the year prior to the swarm determined using the Keck network [*Wilcock et al.*, 2004]. (b) SOSUS seismicity 2005 swarm. Map of seismicity detected in real time during the late February 2005 swarm by the Navy hydrophone array (SOSUS) (red dots) for events occurring during the first 5 h of year days 56 and 58–62. Also illustrated is the area covered during the event response cruise on 6 March 2005, showing tow-yo tracks (white lines), vertical CTD casts (blue squares), and a bottom camera tow (pink line). (c) Keck network seismicity 2005 swarm. Map of seismicity during the late February 2005 swarm determined using the Keck network [*Patel*, 2007]. In each map the Endeavour vent fields (green stars) and Keck seismometers (white triangles) are shown and the four regions of the swarm are outlined with light black rectangles. Epicenters in Figures 2a and 2c were determined using the "genloc" algorithm [*Pavlis et al.*, 2004] and are thus directly comparable.

sealed boreholes (IODP CORK sites) are used to understand subsurface tectonic and magmatic processes. We infer that a magmatic intrusion at the northern tip of the Endeavour axis results in stress changes at the Endeavour–West Valley OSC causing tectonic deformation and possible dike propagation on the opposing limb of the OSC. We attribute the delay in the seismic and hydrothermal vent field perturbations to a hydrologic pressure pulse that diffuses away from the magma intrusion.

2. Previous Swarms and Hydrothermal Perturbations at the Endeavour Segment

[7] The Juan de Fuca ridge is an intermediate spreading rate (~60 mm/yr full rate) mid-ocean ridge (MOR) that forms the boundary between the Juan de Fuca and Pacific plates (Figure 1). The Juan de Fuca ridge consists of seven spreading segments separated by overlapping spreading centers (OSCs) that migrate along axis through time. Our study is focused at the Endeavour segment located near the northern end of the Juan de Fuca ridge. To the south and north the Endeavour forms left-stepping OSCs with the Cobb and West Valley segments, respectively. The West Valley OSC developed recently, about 200,000 years ago, with a 20 km westward ridge jump from Middle Valley [*Karsten et al.*, 1990]. The OSC overlap basin forms a depression called Endeavour Valley. Three seamount chains dominate the bathymetry west of the Endeavour segment. The northernmost (Heck) seamount chain intersects the Endeavour–West Valley OSC. The central portion of the Endeavour segment hosts five high-temperature hydrothermal fields that have been studied extensively over the last two decades [*Kelley et al.*, 2002] (Figure 2). These vents are spaced 2–3 km apart along the ridge axis and are driven by heat from an axial magma chamber (AMC) located 2.1–3.3 km below the seafloor [*Van Ark et al.*, 2007].

[8] The center of the Endeavour segment and the OSCs that form the northern and southern terminus of this segment are regions of ongoing elevated earthquake activity. Several earthquake swarms have been documented [*Bohnenstiehl et al.*, 2004; *McClain et al.*, 1993] and background seismicity levels are high [*Wilcock et al.*, 2002, 2004, 2009]. Figure 2a shows the spatial distribution of epicenters obtained using the Keck network for events that occurred throughout the year from the summer of 2003 to that of 2004 [*Wilcock et al.*, 2004]. Two large earthquake swarms occurred at the center and

along the southern half of the Endeavour segment in June 1999 and January 2000. These two swarms were followed in late February of 2005 by a large swarm at the northern end of the Endeavour segment. The U.S Navy's Sound Surveillance system (SOSUS) detected all three of these seismic swarms in real time [*Bohnenstiehl et al.*, 2004; *Dziak et al.*, 2007].

[9] The June 1999 earthquake swarm was centered near 47°49′N and lasted 5–11 days [*Johnson et al.*, 2000]. The epicentral locations migrated ~12 km to the south at a rate of 0.3 m/s = 1.1 km/h This migration rate is similar to the lateral dike propagation rates measured by the migration of seismicity at other volcanoes: Krafla (0.1–0.5 m/s = 0.3–1.8 km/h) [*Einarsson and Brandsdottir*, 1980], Kilauea (0.2 m/s = 0.7 km/h) [*Koyanagi et al.*, 1988], Co-Axial (0.3 m/s = 1.1 km/h) [*Dziak et al.*, 1995], North Gorda (0.6 m/s = 2.2 km/h) [*Fox and Dziak*, 1998] and Axial volcano (0.2–0.9 m/s = 0.7–3.2 km/h) [*Dziak and Fox*, 1999]. Chemical analysis of the Endeavour vent fluid samples, collected three months after the swarm, showed an increase in magmatic volatiles (CO_2 and He) compared to the previous year [*Lilley et al.*, 2003]. The along-axis migration of seismicity and the increase in magmatic volatiles suggest that a magmatic intrusion occurred during the June 1999 swarm.

[10] The June 1999 seismic swarm coincided with pressure transients observed in permeable formations monitored by regional IODP borehole sensors. *Davis et al.* [2001] model these pressure transients as a combination of instantaneous internal plate deformation due to extension at the ridge axis and lateral water flow in the crust resulting from strain-induced fluid pressure gradients. The rate at which the pressure transients dissipate is controlled by the regional-scale permeability of the upper igneous crust. The initial amplitude of the borehole pressure transients can be used to constrain the instantaneous strain. Modeling of the pressure transients suggested a dike injection with 12 cm of strain, where the length and depth extent of the dike is 40 km × 3 km [*Davis et al.*, 2001]. At full seismic efficiency a dislocation of 12 cm would be equivalent to a magnitude >5.7 earthquake. However, the earthquake that initiated the 1999 swarm is a 4.6, suggesting that 97% of the displacement was due to aseismic spreading [*Davis et al.*, 2001].

[11] The subsequent swarm, in January 2000, showed no migration, a shorter duration of seismicity, greater mean magnitude, and fewer events, suggesting a tectonic origin, possibly in response to extension caused by the dike propagation during the June 1999 swarm [*Bohnenstiehl et al.*, 2004]. Following the 1999 and 2000 earthquake swarms there was a reduction in gradients in fluid temperatures and chemistry across the Main Endeavour Field, suggesting modification of the subsurface plumbing system [*Lilley et al.*, 2003; *Seyfried et al.*, 2003].

[12] In contrast to the 1999 and 2000 swarms, which were located in the central and southern regions of the Endeavour segment, the late February 2005 seismic swarm occurred at the northern end of the Endeavour segment. It was detected in near–real time by the SOSUS Navy hydrophone array (Figure 2b shows the SOSUS-derived epicenters and Figure 2c shows epicenters obtained using the Keck array). This swarm was interpreted as having a magmatic component because of the large number of earthquakes and lack of clear foreshock-aftershock sequence (Omori decay rate). There was also an indication that the events migrated southward [*Dziak et al.*, 2007]. A rapid response cruise found no evidence for a seafloor eruption or its water column expression (Cruise report available at the NOAA Web site: http://www.pmel.noaa.gov/vents/acoustics/seismicity/nepac/endeav0205.html) (Figure 2b). However, in the summer of 2005, CO_2 levels in the Main Endeavour vent field were significantly elevated above those measured in 2004 and 2006, but CO_2 levels at Mothra and Sasquatch did not change [*Love*, 2008]. This swarm is unique in that a local seismometer network, the Keck array, was in place providing a lower detection threshold and allowing us to obtain more accurate epicentral locations.

3. Microearthquake Experiment

[13] The Keck seafloor seismic array was located ~10–40 km to the south of the February 2005 swarm (Figure 2) and was operated from 2003 to 2006. The Keck array comprised eight seismometers deployed about 3 km apart along the 10 km long section of the ridge that includes the Endeavour vent fields. Unlike previous microearthquake experiments that used freefall ocean bottom seismometers, the Keck seismometers were deployed below the seafloor by a remotely operated vehicle (ROV) to ensure good coupling and to minimize ocean current generated noise.

[14] The instruments were developed collaboratively by Monterey Bay Aquarium Research Institute (MBARI) and the University of California, Berkley,

Table 1. Swarm Characteristics by Region

Region of the Swarm	Typical Number of Arrivals		Typical Arrival Time Errors		Genloc Location Uncertainties			Grid Search Location Errors			Moment Release		Gutenberg-Richter Relationship	
	Mean Number of *P* Arrivals	Mean Number of *S* Arrivals	Mean *P* Arrival Time Error (s)	Mean *S* Arrival Time Error (s)	Semimajor Axis (km) (Median ± SD)	Semiminor Axis (km) (Median ± SD)	Strike (deg) (Median ± SD)	Semimajor Axis (km)	Semiminor Axis (km)	Strike (Degrees From North)	Not Including the Six Largest Events (10^{23} dyn cm)	Including the Six Largest Events (10^{23} dyn cm)	*b* Value Estimate	Magnitude of Completeness
Box 1: Endv Seamount	3.4	3.3	0.01	0.04	4.5 ± 2.0	0.9 ± 0.3	278 ± 7	4.4 ± 2.0	0.6 ± 0.3	280 ± 40	0.04	0.04	2.0	2.0
Box 2: N. Endv	3.1	3.8	0.03	0.05	3.5 ± 1.5	0.9 ± 0.5	297 ± 13	2.9 ± 2.2	0.6 ± 0.4	300 ± 15	0.42	0.42	2.5–3.0	1.9
Box 3: SW Endeavour Valley	3.8	3.9	0.04	0.07	2.6 ± 1.7	0.9 ± 0.4	277 ± 24	0.9 ± 1.7	0.4 ± 0.5	315 ± 55	1.06	20.96	1.5	1.8
Box 4: Vent Fields	3.8	3.9	0.02	0.03	0.3 ± 0.3	0.2 ± 0.2	337 ± 43	0.6 ± 2.1	0.3 ± 0.5	0 ± 30	0.07	0.07	1.5	1.3

and included seven short-period three-component seismometers [*Stakes et al.*, 1998] and one three-component broadband seismometer [*Romanowicz et al.*, 2003]. The short-period instruments consisted of three orthogonal Mark Products L-28B geophones that are sensitive in the frequency range of 1 to 50 Hz and were sampled at 128 Hz. Five of the short-period seismometers were inserted into horizontal core holes drilled by an ROV-mounted diamond drilling system into basement outcrops, including individual pillow mounds. At two sites (KESE and KESW) the short-period seismometers were placed into a 69 kg concrete block that was set a few centimeters into sediments. The broadband seismometer was a three-component Guralp CMG-1T and is sensitive in the frequency range of 2.8 mHz (360 s) to ~20 Hz; during the period of this study the data were sampled at 50 Hz. The broadband seismometer was buried ~50 cm in the sediments inside a PVC caisson that was infilled with 0.8 mm diameter glass beads.

4. Methods

4.1. Arrival Time Data

[15] The Keck seismic array recorded local seismic *P* and *S* waves in contrast to the regional acoustic *T* phases used by SOSUS. For this time period, we primarily used data from 5 stations as one short-period data recorder flooded (KESQ) and two of the short-period sensors malfunctioned with greatly reduced sensitivity so they only recorded the largest events (KEMF and KEMO). We used an automatic triggering algorithm to identify arrivals. A typical event had three to four *P* and three to four *S* arrivals. The *P* and *S* wave arrival times were handpicked from 21 February through 5 March 2005 (year days 52 to 64) with a 3 Hz high-pass filter [*Patel*, 2007]. Due to the volume of data, travel time errors were not assigned to the bulk of the arrivals (total of 49,028 arrivals). Instead, arrival time errors were manually assigned for subsets of representative events in each of the regions that were active during the swarm (Table 1).

4.2. Epicentral Locations

[16] Over 6000 epicentral locations were initially obtained from travel time measurements [*Patel*, 2007] using the "genloc" algorithm in the Antelope software (Figure 2c) [*Pavlis et al.*, 2004]. The velocity model was taken from *Wilcock et al.* [2002] and is based on the average upper crustal velocity struc-

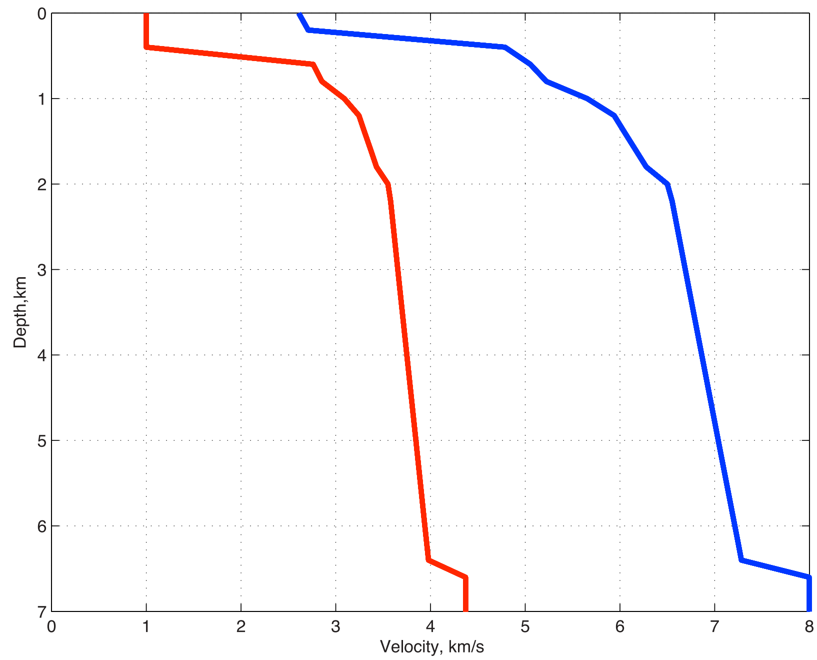

Figure 3. Compressional and shear velocity models used in the epicentral determinations (blue and red lines, respectively).

ture obtained by an earlier refraction experiment [*Cudrak and Clowes*, 1993] with a Moho depth estimated from reflection data [*Rohr et al.*, 1988]. The velocity model included a low-velocity layer 2A and a Vp/Vs ratio of 1.83, except in the upper 400 m of the model where Vs was set to 1.0 km/s (Figure 3).

[17] We used the grid search method of *Wilcock and Toomey* [1991] to obtain epicentral locations and confidence intervals using the *F* statistic (Figures 4–8). This method is preferable for locating earthquakes outside of a seismic array, since it provides a more robust estimate of epicentral uncertainties. The grid spacing was 200 m, it was centered on the Main Field and it extended 30 km east, 20 km west, 20 km south and 67 km north. We fixed all the earthquake depths to 3 km, yielding three degrees of freedom for each event. Based on the subsets of manually assigned arrival time errors, we used estimated *P* and *S* arrival time errors of 0.05 and 0.1 s, respectively.

[18] The location errors are reported for a *F* statistic probability of 40%, which corresponds to a one-sigma error ellipse in two dimensions. Typical error ellipses have the major axis in the azimuthal direction and range from 4.5 km EW by 0.6 km NS for distant events to 0.6 km NS by 0.3 km EW for events within the array (Table 1). These estimates do not include the uncertainty in the V_P/V_S ratio, which primarily affects the distance to the event; an error of ±5% in the V_P/V_S ratio changes the epicentral distance by ±4–5 km, ±1 km, and ±0.1 km at 40 km, 10 km, and 1 km range, respectively. The error introduced by fixing the earthquake depth is estimated by comparing the locations determined for a 3 km focal depth with those for focal depths of 0 km and 6 km. This error is largest in the radial direction and typically ranges from 1.7 km for distant events at the Endeavour Seamount to 0.5 km for events within the array at the Endeavour vent fields. Combining these three sources of error gives error ellipses that are 4.5 km EW by 4.5 km NS for distant events to 0.6 km NS by 0.5 km EW for events within the array (Figure 4).

4.3. Source Parameters

[19] Seismic moments were calculated from *P* and *S* wave spectral amplitudes [*Brune*, 1970; *Hanks and Wyss*, 1972] using methods and parameters developed for oceanic seismic data (Table 2) [*Toomey et al.*, 1988; *Tréhu and Solomon*, 1983; *Wilcock et al.*, 2009]. The seismic moment of an earthquake is the median value of that determined for each of the picked arrivals for that event (Figure 9).

[20] The seismic moment, M_o, was converted to the local magnitude, M_L, using the relationship (where

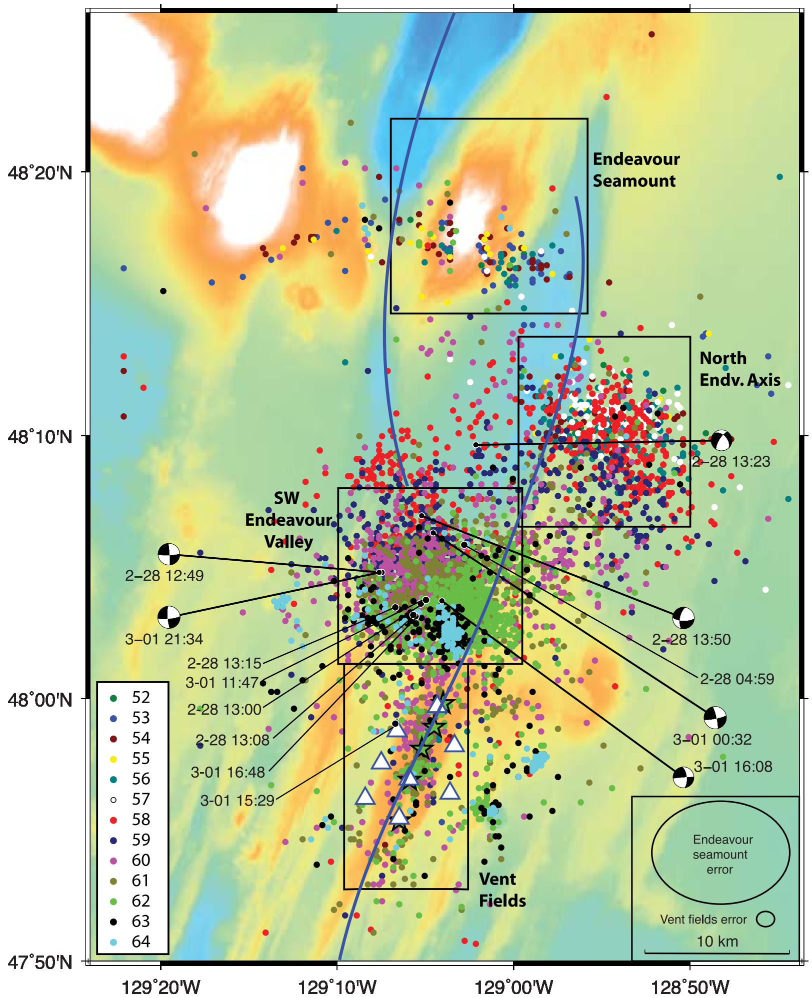

Figure 4. Temporal evolution of seismicity. Map of the epicentral locations for the late February 2005 seismic swarm plotted by year day (color coding shown in the bottom left). Epicentral locations are determined by the grid search method [*Wilcock and Toomey*, 1991]. Focal mechanisms and UTC times of the six largest events detected by the PGC are plotted with locations determined by arrival times on the Keck seismometers. The locations and times of the seven clipped events are also marked in black. The Keck seismometers (white triangles) and Endeavour vent fields (green stars) are shown. The ridge axes are blue lines, and the regions of the swarm are outlined in black rectangles.

M_o is in units of dyn cm) [*Thatcher and Hanks*, 1973]:

$$M_L = \frac{2}{3}(\log_{10} M_0 - 16).$$

This was used to determine the Gutenberg-Richter relationship from plots of the logarithm of the cumulative number of earthquakes above a certain magnitude as a function of that magnitude (Figure 10). We visually estimated the slope or b value as well as the cutoff magnitude for each region of the swarm (Table 1).

4.4. Large Events From PGC Catalog

[21] Source parameters (origin time, epicentral location, moments and magnitudes) of the 6 largest events that occurred during the swarm (local magnitudes 3.7 to 4.4) were obtained from the Pacific Geoscience Center (PGC) [*Ristau et al.*, 2003]; four of these events also appear in the Global Centroid Moment Tensor (CMT) catalog (http://www.globalcmt.org/) (Figures 4–9). Focal mechanisms are strike-slip with north-south right-lateral or east-west left-lateral motion. To more accurately locate the six largest events, their arrivals were picked in the Keck seismic data and the events were relocated using the grid search algorithm. While these earthquakes clipped the Keck seismometers, they were large enough to be recorded on the stations with reduced sensitivity, KEMO and KEMF. As a result we were typically able to pick six P waves and two S waves for each event. The average one-sigma

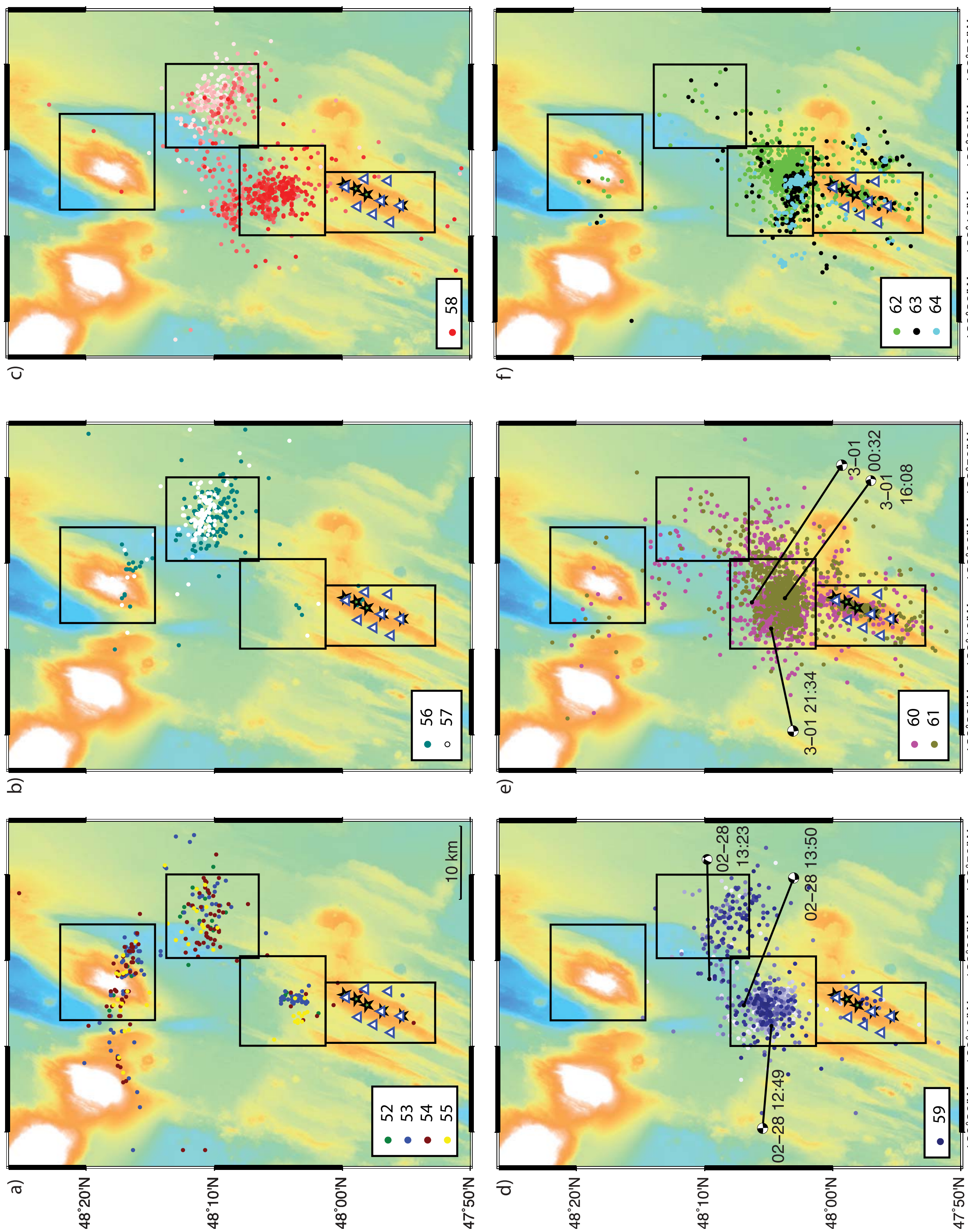
a)
b)
c)
d)
e)
f)
48°20'N
48°10'N
48°00'N
47°50'N
129°20'W
129°10'W
129°00'W
128°50'W
10 km
52
53
54
55
56
57
58
59
60
61
62
63
64
02–28 12:49
02–28 13:23
02–28 13:50
3–01 21:34
3–01 00:32
3–01 16:08

Figure 5

Event Time	Grid search				PGC analysis			Global CMT catalogue		
yearday yr-mo-day hr:min:sec	Lat	Lon	Error (km x km, strike of major axis)	# P-, S-phases	Moment, 10^{23} dyne-cm	M_L	Focal mechanism	Moment, 10^{23} dyne-cm	Mag	Focal mechanism
59 2005-02-28 12:49:21	48.0799	-129.1241	0.9 x 0.2 63°	4P, 2S	3.8	4.2		3.51	Mw = 5.0, mb = 5.0, Ms = 4.2	
59 2005-02-28 13:23:45	48.1608	-129.0356	1.8 x 0.4 77°	6P, 2S	1.6	3.7				
59 2005-02-28 13:50:22	48.1158	-129.0866	0.8 x 0.4 76°	6P, 2S	3.6	4.2		3.10	Mw = 4.9, mb = 4.8, Ms = 4.8	
60 2005-03-01 00:32:20	48.1051	-129.0759	1.1 x 0.2 68°	6P, 2S	6.1	4.0		4.05	Mw = 5.0, mb = 5.0, Ms = 4.8	
60 2005-03-01 16:08:27	48.0619	-129.0678	0.4 x 0.1 349°	6P, 1S	1.8	3.7				
60 2005-03-01 21:34:26	48.0799	-129.1268	0.5 x 0.4 315°	6P, 2S	4.6	4.4		4.45	Mw = 5.0, mb = 4.9, Ms = 4.9	

Figure 6. The six largest events of the swarm. The times of the earthquakes and their locations are determined using the Keck seismic data and the grid search method. The moments and focal mechanisms were obtained from both the Pacific Geoscience Center and from the Global Centroid Moment Tensor catalogue. Times are in UTC.

location error ellipse is 1 km × 0.6 km with a major axis strike of 295°.

[22] For the six largest earthquakes, we used the moments as determined by the PGC in our moment catalog. A search of the Keck seismic data found 7 other events that were clipped on some of the instruments (Figure 4). We confirmed that these events were adequately picked and located using the Keck seismic data. Since the waveforms are clipped the moments and magnitudes of these seven additional events may be in error, however, we found that their magnitudes are consistent relative to the six large events and the remainder of the catalog (Figure 9b).

5. Results

5.1. Complex Space-Time Pattern

[23] The February 2005 seismic sequence consists of three temporal subgroups that we define on the basis of changing event rate. The largest swarm initiates on year day 58 and lasts till year day 64, seismicity rates are 20–100 events per hour. It is preceded by two other distinct seismicity increases. The first occurs between days 52 and 55 and consists of an increase in the seismicity rate relative to the background (20 events per day compared to 0.5 event per day). The second occurs on days 56 to 57 with seismicity rates of 5–30 events per hour. For ease of discussion we refer to these three episodes as the day 52–55 swarm, the day 56–57 swarm and the day 58–64 swarm. We envision that this entire seismic sequence has one common origin.

[24] Our analysis shows that this seismic sequence is spatially and temporally complex. The seismic activity generally moves from north to south but there is no clear linear migration (Figure 9a). Epicentral locations are color coded by year day (Universal Time Coordinates, UTC) in Figure 4 and as a temporal sequence of maps in Figure 5. While, SOSUS found a swarm in the Endeavour Valley as well as elevated seismicity at the intersection of the southern West Valley segment and the Heck seamount chain (Figure 2b), we resolve four regions of activity that evolve over time. These regions are labeled from north to south as follows (Figures 1 and 4): (1) Endeavour Seamount, at the northern

Figure 5. A temporal sequence of seismicity color coded as in Figure 4, for the following year days of 2005: (a) days 52–55, (b) days 56 and 57, (c) day 58, (d) day 59, (e) days 60 and 61, and (f) days 62–64. For days 58 and 59 the intensity of the color increases as the day progresses. The ridge axes, regions of the swarm, seismometers, and vent fields are also shown as in Figure 4.

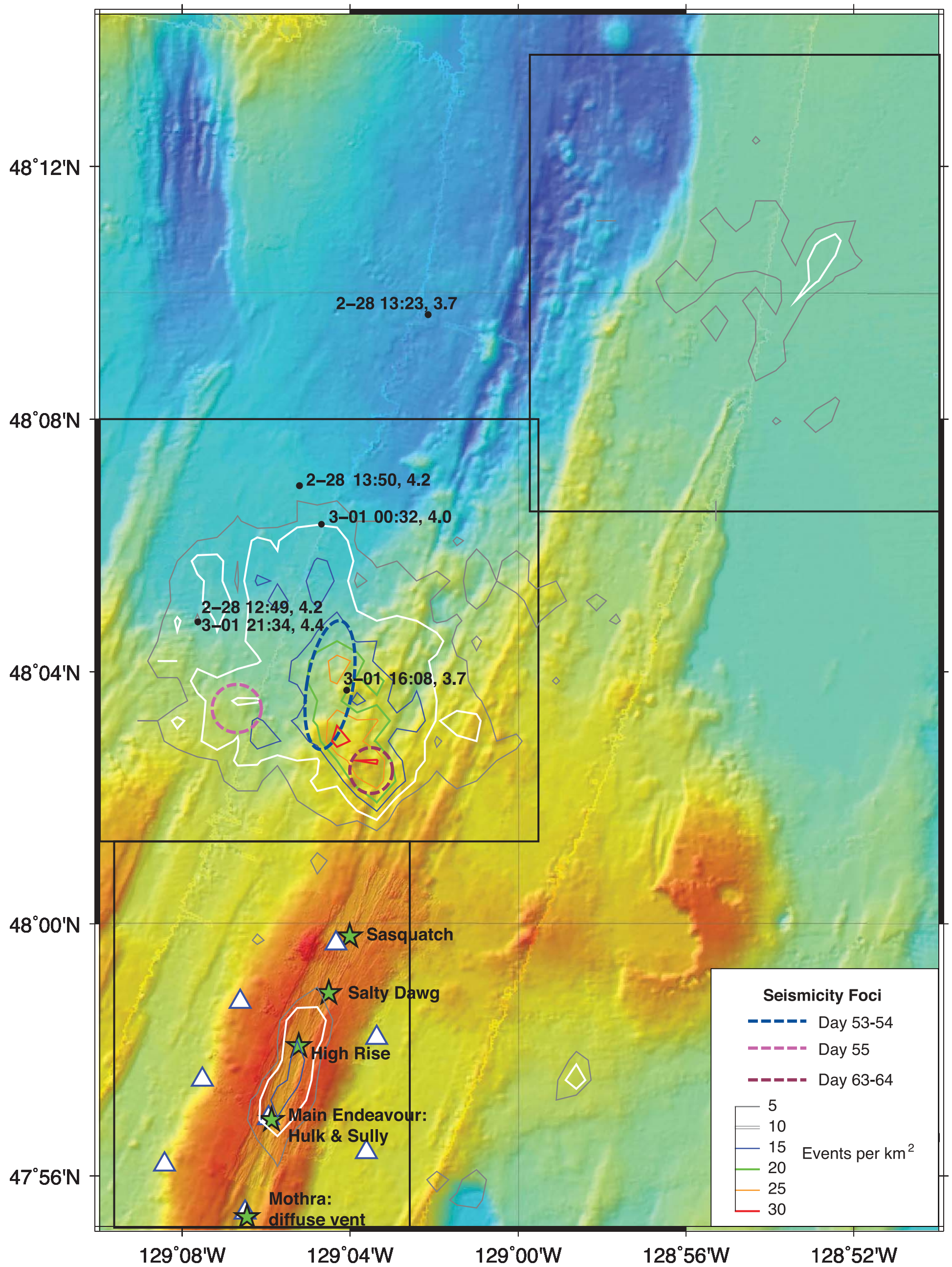

Figure 7. Relationship of seismicity to seafloor morphology. High-resolution EM300 and ABE seafloor bathymetry map (courtesy J. Delaney and D. Kelley, University of Washington) with contours of earthquake density (increments are indicated in the legend). The Keck seismometers and vent fields are shown as in Figure 4. The vent fields are named and indicate the location of the vent structures discussed in the text. Dashed lines show seismicity foci as described in the legend. The six large, strike-slip events are shown by black dots labeled with the date and time and local magnitude from the PGC catalog (Figure 6).

end of the Endeavour–West Valley OSC; (2) northern Endeavour axis, along the northeast boundary of the OSC; (3) southwest Endeavour Valley, along the southwest boundary of the OSC; and (4) vent fields, at the center of the Endeavour segment. Figure 8 shows the number of events per hour for the entire swarm and within each of the four regions. The temporal evolution of the latitude, magnitude, cumulative number of events and cumulative moment is shown in Figure 9.

[25] Prior to the main day 58–64 swarm (during days 52–55) there are increased levels of seismicity

 10.1029/2010GC003264

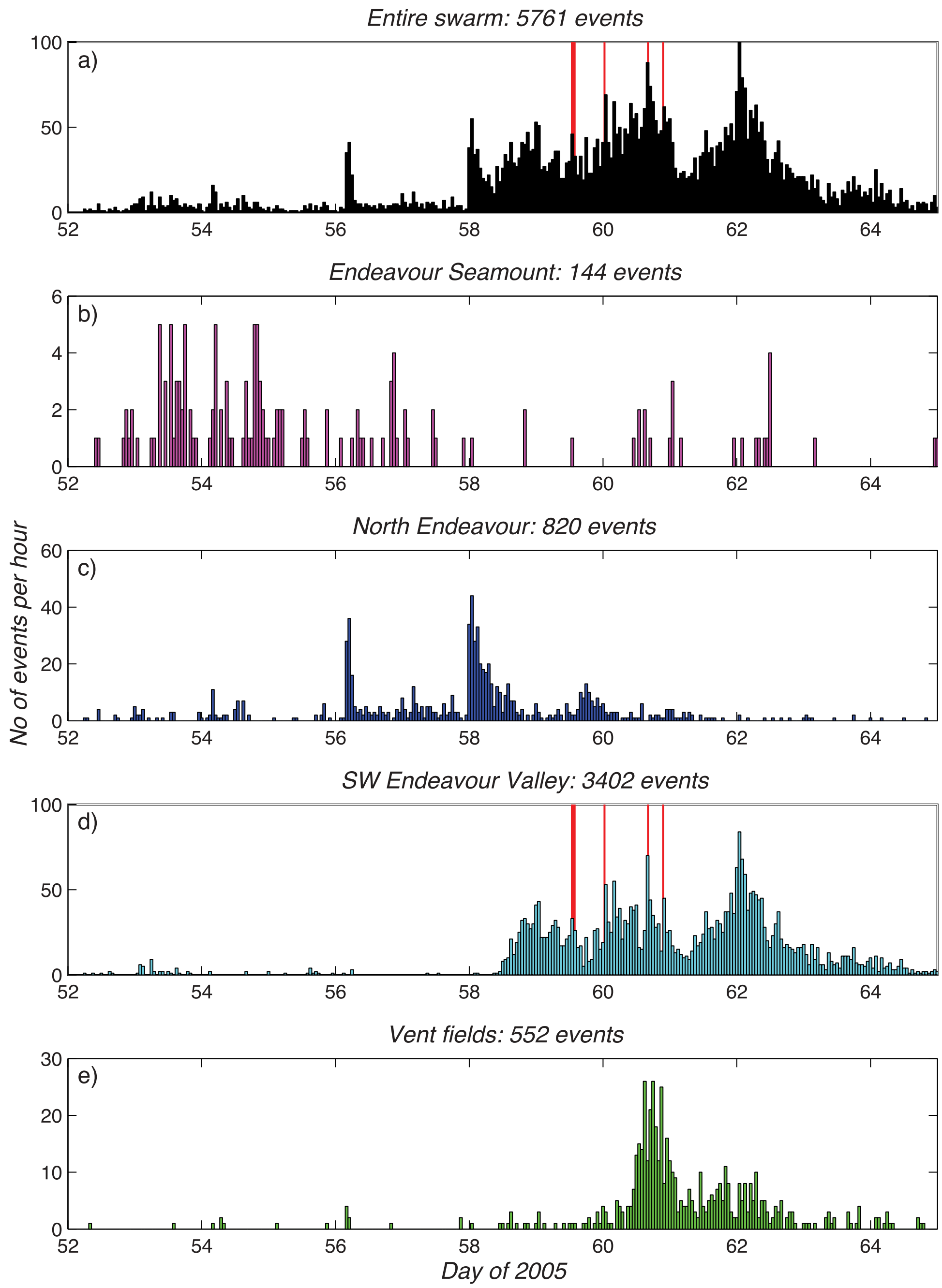

Figure 8. Seismic activity through time. Histograms of the number of events per hour for (a) the entire swarm, (b) the Endeavour seamount region, (c) the northern Endeavour axis region, (d) the southwest Endeavour Valley region, and (e) the vent fields region. The times of the six large, strike-slip earthquakes that occur in the southwest Endeavour Valley region are shown as red vertical lines.

around the entire OSC: near Endeavour Seamount, in the southwest Endeavour Valley and on the northern Endeavour ridge (Figure 5a). The short day 56–57 swarm occurs on the northern Endeavour ridge 2 days prior to the start of the main swarm (Figure 5b). The main, day 58–64 swarm initiates at the northern Endeavour axis (Figure 5c). After 11 h the main swarm jumps to the southwest Endeavour Valley, about 10 km to the southwest (Figures 5c–5f). Most of the seismic energy of this swarm is released within the southwest Endeavour Valley region (Table 1) and this region contains the six large strike-slip earthquakes. The swarm also triggers seismicity beneath the vent fields (~15 km away) about 2.5 days after the swarm's onset on day 58 (Figures 5e and 5f).

Table 2. Parameters Used in Seismic Moment Calculation

Parameter	Value
P window relative to arrival pick (s)	−0.2 to 0.4
S window relative to arrival pick (s)	−0.4 to 0.8
P wave frequency limits for moments (Hz)	4–10
S wave frequency limits for moments (Hz)	4–10
V_P (km/s)	6.5
V_S (km/s)	3.7
Density (g/cm^3)	3.0
Average P wave radiation coefficient	0.42
Average S wave radiation coefficient	0.59
Seafloor interaction correction for P waves[a]	1.5
Seafloor interaction correction for S waves[a]	0.7
Near- and far-field Q_P	30, 500
Near- and far-field Q_S	50, 400
Range at which Q changes from near- to far-field value (km)	1.5

[a] *Toomey et al.* [1988].

[26] Seismic b values indicate the relative proportion of small to large earthquakes and can be diagnostic of tectonic (values of ~1) versus magmatic (values above 1) processes. For all parts of this seismic sequence the b values are greater than one (for the entire sequence $b \sim 2.0$) (Figure 10). This is typical of earthquakes in volcanic and hydrothermal regions [*Bohnenstiehl et al.*, 2008; *Wiemer and Wyss*, 2002].

5.2. Increased Seismicity Rates: Days 52–55 and Day 56–57

[27] During days 52–55, prior to the day 58–64 swarm, seismicity increases around the edges of the OSC (Figures 5a and 7). In the southwest Endeavour Valley region this seismicity is focused in a region of quasi ridge-parallel volcanic edifices seen in seafloor bathymetry (Figure 7). Early on day 53, 20–30 events (M_L = 1–2.2) are focused on two volcanic edifices (dark blue dashed oval in Figure 7) in the southwest Endeavour Valley region. This activity is accompanied by 10–20 events diffusely located at the northern end of the Endeavour segment. On day 54, an additional 20–30 events occur at the northern end of the Endeavour segment. This is followed on day 55, by another ~10 events located at a different small, ~2–3 km, circular seafloor edifice (yellow events in Figure 5a and pink dashed circle in Figure 7) in the southwest Endeavour Valley region.

[28] During days 52 to 55, activity also occurs near the Endeavour seamount (Figures 5a and 8b) that is distinctly elevated compared to background levels (Figure 2a); this activity defines the location of the box for this region (Figure 4). During the entire previous year there were 173 events in the Endeavour seamount region (Figure 2a). In contrast during days 52 to 55 there are up to 90 events in this region, with increased activity late in day 53 and on day 54 (Figure 8a). This activity continues into day 56 and then dies off. A magmatic process is suggested by a b value of ~2 (Figure 10c). Note that the detailed spatial distribution of epicenters at Endeavour Seamount is uncertain due to higher uncertainties at this distance from the array (Table 1).

[29] The small day 56–57 swarm on the northern end of the Endeavour segment marks a ramp up in activity that follows the initial increases in seismicity around the OSC edges (Figures 4, 5b, 8c, and 9). This activity consists of over 100 events during 3 h early on day 56 with a maximum magnitude of about 3. During the remainder of days 56 and 57, the seismicity rate is about 5 events per hour (Figure 8c).

5.3. Initiation of the Day 58–64 Swarm: Northern Endeavour Ridge

[30] We refer to the day 58–64 activity as the main swarm. The main swarm initiates at 0015 UT on day 58 in the same area on the northern Endeavour axis as the day 56–57 swarm but with somewhat higher levels of seismicity (40–50 events per hour) (Figures 4, 5c, and 8c). The seismicity of both the day 56–57 and day 58–64 swarms is located east of where seismicity occurred during the previous year (Figure 2a). The northern Endeavour region is active during the first 11 h of the main swarm. Initially seismicity is spread throughout the northern Endeavour region, but the activity may switch off progressively from north to south; the maximum latitude of seismicity decreases at a rate of 0.07°/d or 0.3 km/h = 0.09 m/s (Figure 9a). The seismicity rate has an Omori-like decay pattern typical of tectonic processes (Figure 8c). However, this swarm does not start with a large earthquake; local magnitudes range up to 3 (Figure 9b). For this part of the seismic sequence, there is a poor fit to the b value model (the possible b value ranges from 1.5 to >2.5) unless we assume that the completeness is limited to magnitudes >2.7, which is inconsistent with the lower magnitude of completeness for the more distant Endeavour seamount region. A magmatic process is suggested since the b value, though uncertain, is greater than 1.

5.4. Latter Part of the Day 58–64 Swarm: Southwest Endeavour Valley

[31] As the seismicity at the northern end of the Endeavour ridge axis starts decaying, seismicity picks up in a new region: the southwest Endeavour Valley. The switch occurs on day 58 about 11 h after

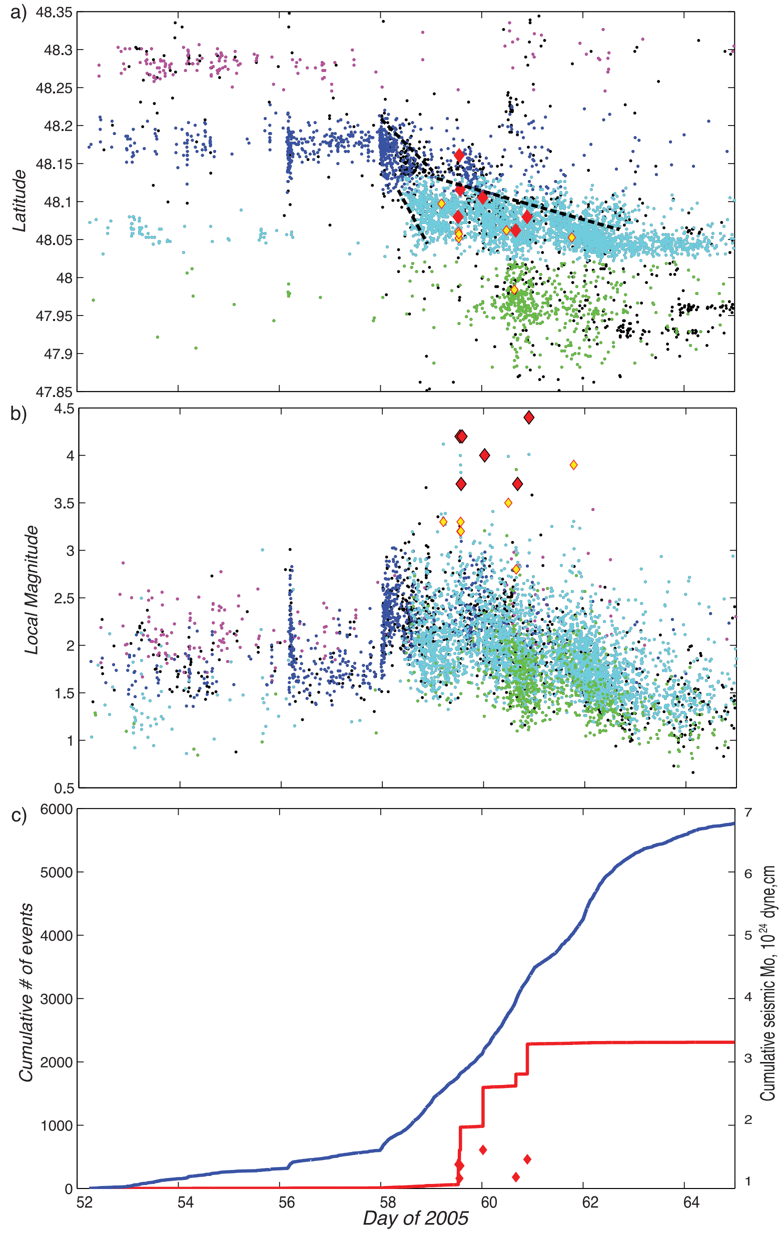

Figure 9. Temporal evolution of the swarm illustrating, as a function of the year day of 2005: (a) the latitude of the events, (b) the local magnitude, and (c) the cumulative number of events (blue line) and cumulative seismic moment (red line). Red diamonds in each plot show the latitude, magnitude, and seismic moment of the six large, strike-slip earthquakes. The latitude and magnitude of the seven additional clipped events are shown with smaller yellow triangles. The dashed lines in Figure 9a show the rates at which the latitude of seismic initiation and shutoff migrate to the south. The events are color coded as follows: Endeavour seamount, pink; northern Endeavour axis, dark blue; southwest Endeavour Valley, light blue; vent fields, green; and all other events, black.

the start of the main day 58–64 swarm and the southwest Endeavour Valley region is active for the remaining 5.5 days of the swarm. The southwest Endeavour Valley appears to be the primary region for which SOSUS hydrophones detect earthquakes (Figure 2b). At first, the activity is located just south of the southern end of the West Valley ridge segment (Figure 5c) and then moves south. The seismicity rate in this region is the highest and varies between 10 and 80 events per hour (Figure 8d). In contrast to the activity on the northern end of the Endeavour segment, activity in this region does not have an Omori-like decay, but appears to wax and wane in 1.5 day cycles.

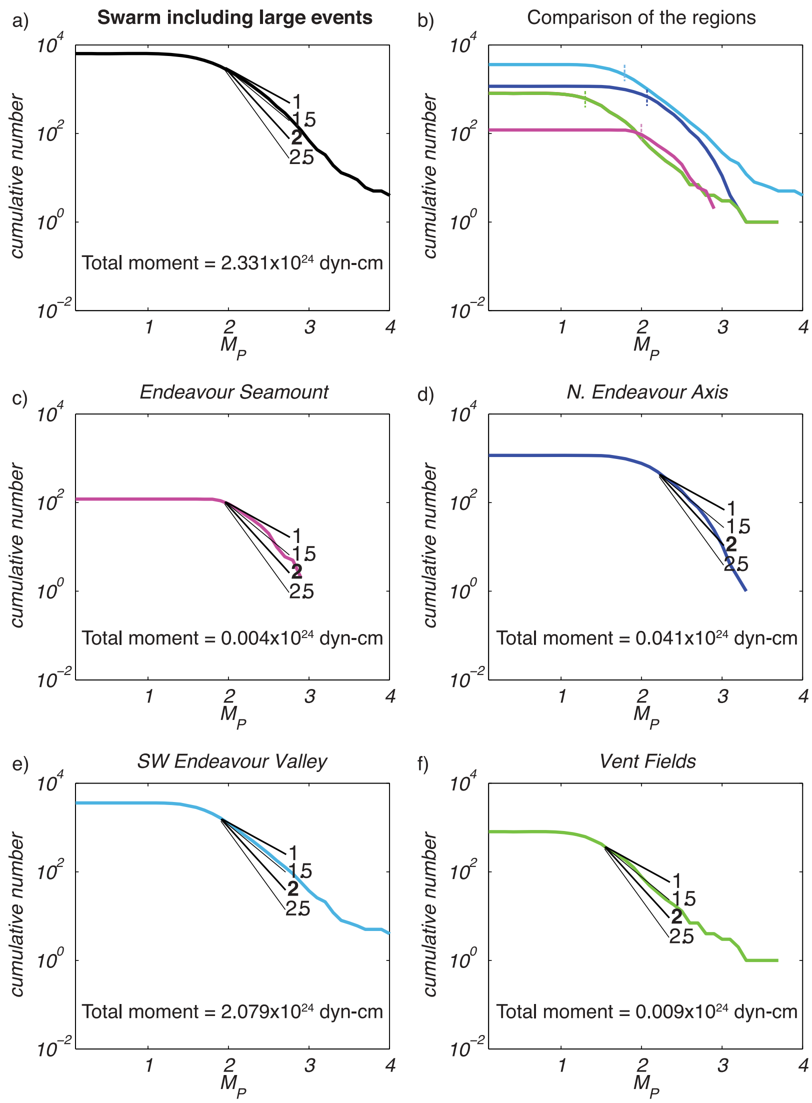

Figure 10. Magnitude distribution of the swarm showing the cumulative number of events whose magnitude is less than or equal to that magnitude. The six large events are included. (a) The entire swarm. (b) A comparison of the four regions color coded as in Figure 9. Estimates of the magnitude of completeness for each region are shown with dashed vertical bars. (c) Endeavour seamount, (d) northern Endeavour axis, (e) southwest Endeavour Valley, and (f) vent fields. For the northern Endeavour region the curved nature of the line makes it difficult to assign a magnitude of completeness; this region is a poor fit to the *b* value model.

[32] The southwest Endeavour Valley region dominates the swarm and includes more than half the seismicity located for the entire sequence. The events in this region are the largest, up to magnitude 4.4, and there are relatively more large events (*b* value ~1.5) (Figure 10). The cumulative moment (21×10^{23} dyn cm^{-1}) is 2 orders of magnitude greater than that of the other swarm regions because all the largest events are located here (the six largest and six of the seven additional clipped events, Figure 4). For the six largest events magnitudes range from 3.7 to 4.4 and moments range from 1.6 to 6.1×10^{23} dyn cm (Figures 4 and 6). The additional seven clipped events also occur during days 59 and 60 and have local magnitudes ranging from 2.8 to 3.9 (Figure 9b).

[33] There is a jump in seismic moment release during the second half of day 59, 1.5 days after the main day 58–64 swarm starts (Figure 9c). The first three large strike-slip events occur within 1 h on day 59 and three of the seven clipped events occur in the half hour between the first two of the six largest events (Figures 4, 5d, and 6). These events do not have aftershock sequences but instead are followed

by a drop in seismicity rates within the southwest Endeavour Valley region (Figure 8d). In contrast, at the northern Endeavour ridge axis these earthquakes are followed by a 6 h increase in seismicity (Figure 8c).

[34] After 2000 UT on day 59, seismicity rates in the southwest Endeavour Valley region increase again. The last three large strike-slip events occur distributed throughout day 60 and their timing appears random relative to the waxing and waning of the swarm (Figures 5e, 8d, and 9). Following the last of these events on day 60 seismicity rates in the southwest Valley region drop (Figure 8c). Then, after the first quarter of day 61, seismicity in this area gradually increases again to a peak rate of about 80 events per hour at the start of day 62. Following this final peak seismicity rates gradually decay to the end of day 64 (Figure 8d). Earthquake magnitudes also decrease as the swarm wanes (Figure 9b).

[35] While the very first earthquakes in the southwest Endeavour Valley region are located to the north, the activity generally spreads southward (Figures 5c–5f). The onset of seismicity migrates south at a rate of ~0.12°/d which is ~0.6 km/h or 0.15 m/s (Figure 9a); this is on the low end of the dike propagation rates cited in the introduction (0.3 to 3.2 km/h). By the end of the swarm, seismicity focuses down to volcanic edifices in the southern part of this region (Figures 5f and 7). This focus is colocated with the fifth large event (on day 60 at 1608 UT, Figure 5e) and is near the locus of earlier activity on day 53 (Figures 5a and 7). Note that while the activity becomes localized in the southern parts of this region, there are additional earthquakes extending to the west (Figure 5f).

5.5. Vent Field Seismicity

[36] Seismicity is triggered within the hydrothermal vent fields ~2.5 days into the main, day 58–64, swarm (Figure 4). The vent field seismicity starts on day 60 at around 1000 UT and reaches rates of about 25 events per hour over 16 h (Figure 8e). The rates remain elevated at about 5–10 events per hour till the end of day 62. The *b* value in this region is about 1.5 (Figure 10). The size of the vent field events is larger than during the previous year (summer 2003–2004) [*Wilcock et al.*, 2009]; 15 events of magnitude 2.5 and larger occur (Figures 9b and 10f). A few of the larger vent field events occur when seismicity starts in the southwest Endeavour Valley region (halfway through day 58). Seismicity extends along the ridge axis from the Salty Dawg vent field to the Main Field (Figures 5e and 5f). The seismicity occurs simultaneously in the entire vent field region with no evidence of propagation. The spatial pattern of this seismicity (Figure 7) matches that during the previous year [*Wilcock et al.*, 2009] with events concentrated between the High Rise and Main Field vents.

6. Hydrothermal and Hydrologic Responses

6.1. Hydrologic Responses

[37] The onset of the main day 58–64 swarm is contemporaneous with changes in formation pressure at sealed seafloor boreholes (IODP drill holes instrumented with CORKs) [*Davis et al.*, 1992]. On the east flank of the ridge, holes 1024C at 25 km and holes 1026B and 1027C both at 100 km, show contraction, while 50 km to the north, hole 857D, at Middle Valley shows dilation (Figures 1 and 11). The passage of the seismic waves from the six large earthquakes is recorded at high frequencies in the borehole pressure records (Figure 11c). To remove pressure fluctuations due to tides we first remove the seafloor pressure from the borehole pressure after applying the loading efficiency at each site, and then remove the tidal component predicted using the MATLAB toolbox t_tide, which uses harmonic analysis to compute tidal coefficients [*Pawlowicz et al.*, 2002]. At the closest sites, 1024C and 857D, the pressure clearly starts changing at the time of the start of the main day 58–64 swarm at the beginning of day 58 (Figure 11). On the east flank pressure increases and the maximum pressure increase declines with distance from the ridge axis (2.8 kPa, 0.15 kPa, and 0.25 kPa at sites 1024C, 1026 and 1027, respectively). In contrast to the pressure increase on the east flank, the pressure drops to the north at site 857D, the maximum pressure drop is −0.4 kPa. At each borehole the pressure anomaly starts when the swarm initiates and the amplitude of the signal continues to grow for 4 to 5 days, i.e., during the duration of the swarm. Curiously, the swarm is followed by a yearlong increase in pressure to the north at Middle Valley (857D) [*Inderbitzen et al.*, 2008].

[38] The February 2005 pressure transients are very similar in both sign and amplitude to the pressure transients associated with the June 1999 swarm that accompanied magma intrusion at the Endeavour ridge axis, which was modeled as 12 cm of extension on a 40 km × 3 km dike [*Davis et al.*, 2001]. This similarity indicates that a crustal deformation event of a similar size and magnitude occurred. How-

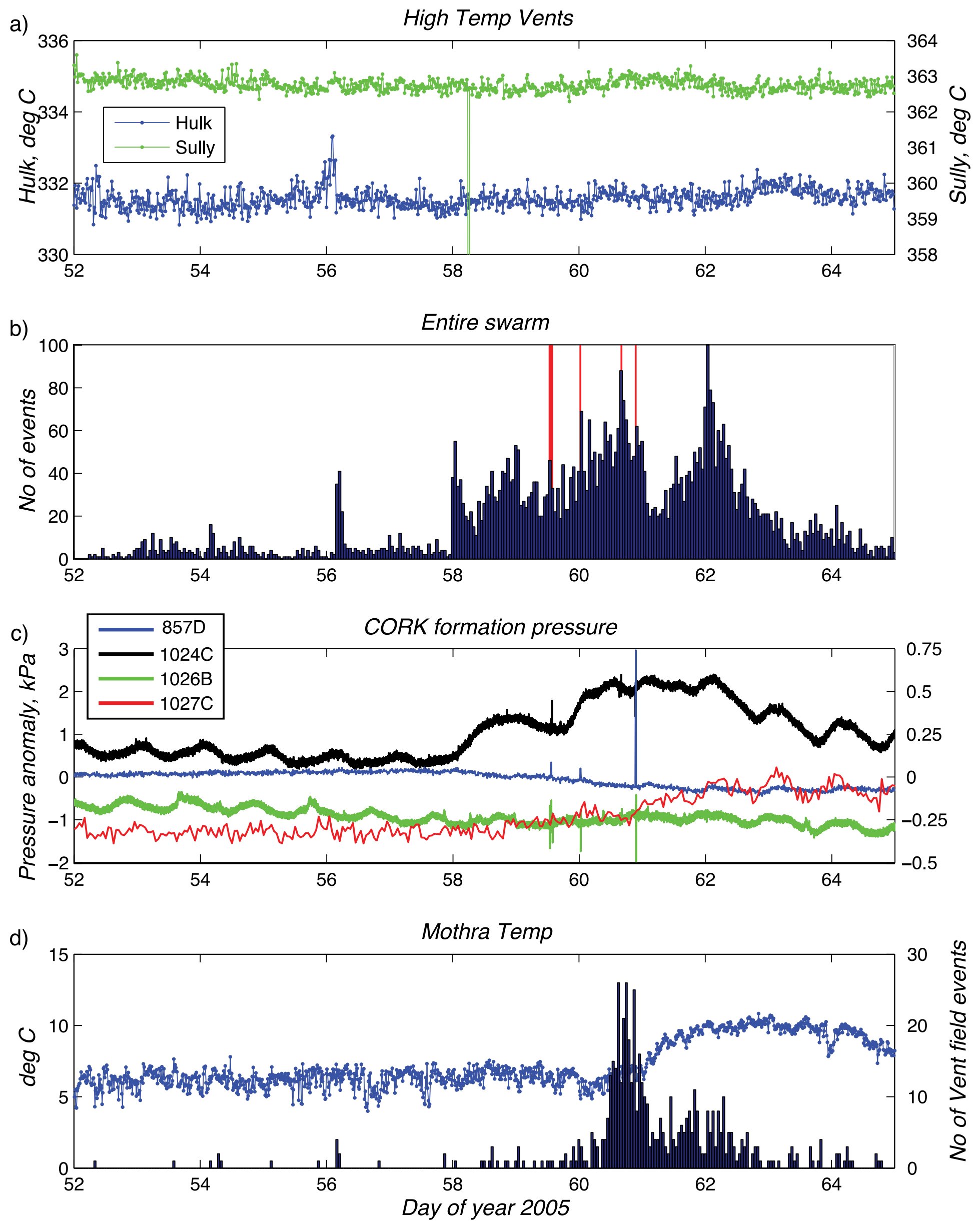

Figure 11. Hydrothermal and hydrologic perturbations during the swarm. Plotted as a function of the day of 2005 are (a) the temperature in the high-temperature Main field vents Hulk (blue) and Sully (green); (b) a histogram of the number of events per hour for the entire swarm showing the six large, strike-slip events as red vertical lines; (c) the detided pressure anomaly in sealed seafloor boreholes shown with variable scaling, where the blue and black lines correspond to the scale on the left and show 857D (blue) and 1024 C (black) and the green and red lines are for the scale on the right and show 1026B (green) and 1027C (red); and (d) the temperature in a diffuse vent field at Mothra (blue line) and a histogram of the seismicity rate in the vent field region.

ever, there are differences in the time to reach the maximum pressure anomaly; the amplitudes of the pressure anomalies grow more gradually for the February 2005 swarm than in June 1999. This may reflect more gradual inflation of the dike in contrast to the 1999 event that began with the largest earthquake, a M_w 4.6 event.

6.2. Hydrothermal Perturbations

[39] The seismicity in the vent fields is concurrent with an increase in diffuse venting temperature (about 4°C) at the Mothra field (Figure 11d) and a coincident change in chemistry. The onset of the day 56–57 and main day 58–64 swarms also coincides

with short-term perturbations to black smoker temperatures in the Main Endeavour field.

[40] At the onset of the day 56–57 and main day 58–64 swarms there are two curious thermal excursions at high-temperature vents in the Main Endeavour field (Figure 11a). The first occurs at Hulk where the temperature increases by 1.5°C (compared to background variations of 0.5°C) over several samples *prior* to the start of the day 56–57 swarm at the northern tip of the Endeavour axis; the sampling interval is 20 min. During the precursory swarm temperatures drop back to normal. Note that in the first 2 h of this precursory swarm there are also 6 earthquakes beneath Salty Dawg in the northern vent fields (Figure 8e). The second thermal excursion is at Sully where temperature in the vent drops to ambient temperature (2.5°C) for one sample a few hours after the start of the main day 58–64 swarm. This single reading may be a bad data point or a momentary change in flow or sensor position, but such effects are not usually observed.

[41] The most robust hydrothermal anomaly that occurs during the seismic sequence is at a diffuse vent in the Mothra field where temperature increases by about 4°C 1.5 days after the start of the main day 58–64 swarm (Figure 11d). This anomaly lasts ~4 days and decays once the swarm terminates. The start of this perturbation coincides with the third of the six largest earthquakes located ~20 km north of the vent (Figure 11b). The seismicity beneath the vent fields peaks in the 2 days during which the temperature gradually increases. Note that the Mothra diffuse vent field is located 3 km south of the primary area of triggered seismicity (Figure 7) and there are only a few earthquakes located near Mothra (Figure 3).

7. Interpretation

[42] The February 2005 seismic sequence included regionally recorded earthquakes and it perturbed seafloor hydrothermal venting and regional-scale formation pressures. Given the duration and magnitude of seismicity the RIDGE2000 program conducted an event response effort [*Dziak et al.*, 2006], which found no evidence of a seafloor eruption. We attribute this seismic sequence to a magma intrusion event at the northern Endeavour ridge axis as evidenced by the crustal deformation inferred from formation pressures, the high *b* values and the temporal and spatial complexity of the seismicity. We infer that seismicity in the southwest Endeavour valley region is caused by fault slip on the opposing limb of the Endeavour–West Valley OSC that may or may not be accompanied by southward dike propagation of the West Valley segment.

7.1. Magmatic Intrusion at the North Endeavour Ridge Axis

[43] We infer that a magma intrusion at the northern end of the Endeavour segment is the dominant process driving the February 2005 seismic sequence. Both the smaller day 56–57 swarm and the initial 11 h of the main day 58–64 swarm are located on the northern Endeavour ridge indicating that an event in this region triggers the seismic sequence (Figures 5 and 8). Seismicity in the northern Endeavour region has a *b* value greater than 1 consistent with a volcanic process. However, the seismicity itself does not require extensive deformation since it is short lived and the net seismic moment in the region is small. Nor does the seismicity require propagation of the volcanic process since there is no clear migration of epicenters at the northern Endeavour (only the shutoff of seismicity appears to migrate southward).

[44] In contrast the timing, magnitude and sign of borehole pressure perturbations require significant crustal extension consistent with a dike intrusion on the northern Endeavour ridge axis. The start of this deformation event, as revealed by the timing of borehole pressure perturbations, is contemporaneous with initiation of the main day 58–64 seismic swarm in the northern Endeavour region (Figure 11). The spatial pattern of the February 2005 borehole pressure transients is consistent with north-south oriented dike injection at the Endeavour segment. The instrument at IODP site 857D is located to the north in the zone of extension in front of the dike tip, thus leading to dilation and a pressure drop. At the same time, pressure increases at the eastern flank sites because these are in compression as the dike expands (IDOP sites 1024C, 1026B and 1027C; Figure 1). The similarity in amplitude of the pressure deviations of the February 2005 event to those of the June 1999 event indicate that the February 2005 extension event involves a similar magnitude of dilatation (on the order of 10 cm) [*Davis et al.*, 2001]. As was true for the June 1999 event, the February 2005 extension is largely aseismic because the magnitude of crustal deformation far exceeds the net seismic moment, observations consistent with the fact that a significant portion of plate spreading occurs aseismically [*Solomon et al.*, 1988]. In fact, the 2005 event is accompanied by even less seismic moment release than the 1999 event, which started

with a magnitude 4.6 earthquake. Furthermore the slow build-up of the pressure transients in 2005 suggests an intrusion that lasts about 4–5 days, while the majority of the seismicity at the northern Endeavour occurs during the first day (day 58).

[45] Together we attribute the seismic and borehole pressure observations to a dominantly aseismic magma intrusion at the northern Endeavour ridge axis. While SOSUS detected seismicity from this period of the swarm, their epicenters are located in the Endeavour Valley (Figure 2b). In spite of this difference in locations, the event response cruise ran their easternmost tow-yo up the Endeavour ridge axis (Figure 2b) and did not find any evidence for a seafloor eruption. Thus we infer that the intrusion did not rupture the seafloor. It is unclear whether this intrusion was a propagating dike because there is no clear epicentral migration. Dike propagation may occur aseismically, but we consider breaking the upper crust ahead of a shallow dike tip without accompanying earthquakes unlikely. It is possible that the magma intrusion and dike propagation were confined to the deeper, more ductile axial crust thus allowing significant crustal extension accompanied by limited seismicity. Because the perturbations to the hydrothermal vents are modest, we think it improbable that magma injected into the sill at the center of the Endeavour segment.

7.2. Faulting and Possible Dike Propagation at the Southwest Endeavour Valley

[46] We infer that the magmatic intrusion at the northern Endeavour ridge triggers slip on faults and possibly also dike propagation on the opposing side of the OSC, in the southwest Endeavour Valley region. The southwest Endeavour Valley region contains more than half the epicenters of this seismic sequence and dominates the seismic moment. Tectonic faulting plays a significant role since the six largest earthquakes of the February 2005 seismic sequence occur in the southwest Endeavour Valley region and have north-south right-lateral or east-west left-lateral strike-slip focal mechanisms (Figures 4 and 5). These events occur ~1.5 days after the crustal extension on the northern Endeavour starts, which we attribute to crustal failure in response to stresses generated by the magma intrusion on the northern Endeavour. During normal evolution of the OSC it is under right-lateral shear, which would cause bookshelf faulting with the opposite mechanism, on north-south left-lateral faults. The observed mechanisms may instead be due to deformation on the southwest boundary of the OSC, possibly the reactivation of normal faults, in response to stress modification by the intrusion on the northeast boundary of the OSC, at northern Endeavour ridge axis. We infer that a response to the stress perturbations of the magmatic intrusion at the northern Endeavour causes the high moment release and diffuse distribution of epicenters in the southwest Endeavour Valley region.

[47] The southwest Endeavour Valley seismicity also has magmatic characteristics that may or may not be indicative of a dike propagating south from the West Valley axis. These magmatic characteristics are the waxing and waning seismic rates, high *b* values, and north to south evolution of seismicity, as well as the association with seafloor volcanic features. Southward propagation of a dike from the West Valley axis along the southwest margin of the OSC basin toward the west flank of the Endeavour segment is consistent with the expected evolution of the Endeavour–West Valley OSC. Over time similar dike propagation events may result in the decapitation of the northern Endeavour ridge axis by the West Valley segment [*Karsten et al.*, 1990]. However, the spatial pattern of the borehole pressure transients are not compatible with northwest-southeast oriented dike injection in the southwest Endeavour Valley, indicating that such a dike propagation event is not the main process driving the February 2005 seismic sequence. Alternatively the north-south migration of seismicity may be the result of progressive cracking and faulting associated with tectonic propagation of the OSC with no magma injection occurring in the southwest Endeavour Valley region.

7.3. Deformation at the Endeavour–West Valley OSC

[48] The complex spatial pattern and lack of, or relatively slow, migration of earthquakes in the February 2005 seismic sequence may result from complex stresses around the OSC. When a dike occurs near the tip of a propagator the stress field will slow propagation. This is because near its tip the crack is being held closed by the stresses associated with opening on the opposing crack [*Pollard and Aydin*, 1984]. As a result dike propagation rates near a segment end will be slower than at a segment center. Furthermore OSC stresses are concentrated in the area between one propagating rift tip and the flank of the opposing ridge axis. It is these stress interactions that cause the tip of the propagating rift to curve toward the opposing segment resulting in

the typical curved shape of OSCs. It appears that the seismicity in the southwest Endeavour Valley region is located in this zone between the propagating West Valley segment and the axis of the opposing Endeavour segment.

[49] *Dziak et al.* [2007] infer that whether a dike erupts onto the seafloor is controlled by the pressure in the magma source and possibly also the crustal stress state. The lower extensional stresses near the OSC rift tips not only result in a lower dike propagation rate but much of the magmatic pressure may be used to overcome crustal stresses and break new pathways. It may be a consequence of the complex OSC stresses, that no seafloor eruption accompanies this magmatic event.

[50] If magma is intruding both the northern Endeavour segment and the southwest Endeavour Valley then magma may be entering the entire OSC region from the mantle. The intersection of the Heck seamount chain with the OSC may be the source of this distributed magmatism [*Dziak et al.*, 2006]. In this scenario, magma intrudes the brittle crust in weakened regions, in particular in the region between the West Valley rift tip and the Endeavour ridge axis. The intrusion on the northern Endeavour is the dominant crustal deformation event. This intrusion initiates the swarm and affects stresses around the OSC causing faults to slip on the opposing side of the OSC and possibly triggering dike propagation to the south from the West Valley segment.

7.4. Triggered Vent Field Seismicity and Hydrothermal Perturbations

[51] The low-temperature vent field at Mothra shows a robust perturbation during the main day 58–64 swarm, while the high-temperature vent fields at the Main Endeavour show only minor deviations even though they overlie the seismicity triggered by the swarm. This may reflect the different hydrology of these two systems. The high-temperature fields are more robustly connected to the thermal boundary layer above the magma chamber, the flow is through the biggest cracks, and temperatures are buffered by the wall rock. The low-temperature vent fields are more sensitive to small changes in crack geometry due to remote changes in stress or strain and so temperatures will respond quickly to changes in the relative proportion of high-temperature fluid and seawater.

[52] We attribute both the triggered vent field earthquakes and the diffuse hydrothermal response to upper crustal stress changes; this is in contrast to the local earthquakes causing the diffuse hydrothermal response. The timing of the vent field seismicity, which peaks while the diffuse vent temperatures are increasing, suggests that upper crustal stress changes affect the hydrology so as to increase the hydrothermal component in the diffuse vent field. Below we discuss several possible mechanisms for generating the observed seismic and hydrothermal perturbations in the diffuse vent fields.

[53] It is possible that the regional stress perturbation associated with the third large earthquake on day 60 at 0032 UT triggers the vent field seismic and hydrothermal perturbations. We think this is unlikely since there is no reason why only this third earthquake would have an effect but not other similar earthquakes. In addition the third event is also not the closest earthquake to the vent fields.

[54] Our favored explanation is that the diffuse hydrothermal changes and the vent field seismicity are driven by a pore fluid pressure perturbation that diffuses away from the main diking event in the upper crustal aquifer. While the borehole pressure anomalies coincide with the start of the main day 58–64 swarm, the vent field perturbations occur after ~2.5 days. The diffusion coefficient for pressure can be approximated by permeability/(viscosity*fluid compressibility). The diffusion distance is approximated by the square root of the product of the diffusion coefficient and time. We use parameters from *Davis et al.* [2001]: the bulk modulus of fluid is 2.4 GPa, the compressibility is the inverse of the bulk modulus, and the viscosity of water is 10^{-3} Pa s. For this swarm the fluid pore pressure increase takes ~2.5 days to diffuse a distance of ~35 km, the distance of the vent fields from the magma intrusion on the northern Endeavour ridge. This implies a diffusion coefficient of ~6 × 10^{3} m^2 s^{-1}. This gives an upper crustal permeability of about 10^{-9} m^2, which is consistent with the higher permeabilities inferred by *Davis et al.* [2001].

[55] It is also possible that the intrusion of magma, or removal of magma from the magma chamber during a diking event, results in a pressure perturbation in the interconnected melt network. The resulting pressure perturbation could diffuse along axis within the magma chamber or underlying mush zone. When this pressure anomaly reaches the magma chamber beneath the vent fields it would induce seismicity in the crust overlying the vents and increase the heat supplied to the hydrothermal system resulting in an increase in the temperature of the diffuse vents. This model requires interconnectivity

between the magma system at the northern Endeavour where the intrusion is taking place and those at the central Endeavour segment beneath the vent fields. Given that the viscosity of melt is higher than that of water, the time for a pressure anomaly to diffuse 20 to 40 km to the Endeavour vent fields will be longer. The observed delay of 2.5 days favors the diffusion of a pressure anomaly in water in the crustal aquifer. However, slower diffusion of pressure within the magma system may explain the observed increase in CO_2 at the Main Endeavour field in the summer of 2005 [*Dziak et al.*, 2007; *Love*, 2008].

8. Summary

[56] The February 2005 seismic sequence occurred near the Endeavour–West Valley OSC at the northern end of the Endeavour segment. The seismic sequence was big enough to cause significant regional events and to perturb the vent fields on the central Endeavour segment as well as seafloor boreholes located ~25–100 km away. The seismic sequence was recorded on a local seafloor seismic network from which we determined the spatial and temporal pattern of epicentral locations and the moments of over 6000 events using seismic *P* and *S* wave arrival times. The seismic sequence starts with increased levels of seismicity around the entire OSC during year days 52–55. During days 56–57 a short swarm occurs on the northern Endeavour ridge. The sequence culminates in the main day 58–64 swarm that starts at the northern Endeavour ridge axis and generally progresses to the south including a jump across the OSC to the southwest Endeavour Valley region after 11 h. Seismicity in the southwest Endeavour Valley region dominates the seismic moment release of the swarm, includes six large strike-slip events (north-south right-lateral or east-west left-lateral), and has a general north to south migration of activity (20 km over 5 days).

[57] We conclude that the main driving process of this seismic sequence is a magma intrusion at the north Endeavour ridge. While seismic activity in the north Endeavour region is short lived, it is significant that the deviations in borehole pressure are contemporaneous with the start of the main, day 58–64 swarm in this location. The magnitude and sign of the borehole pressure perturbations are consistent with magma intrusion at the northern Endeavour ridge and indicate considerable crustal extension starting at this time, the majority of which is aseismic since the cumulative seismic moment for the northern Endeavour region is small. A volcanic process in this region is supported by the absence of large earthquakes and *b* value greater than 1.

[58] Furthermore, we infer that the magmatic intrusion at the northern Endeavour ridge triggers slip of faults and possibly also dike propagation on the opposing side of the OSC, in the southwest Endeavour Valley region. Seismicity in the southwest Endeavour Valley region dominates the seismic moment release of the swarm and faulting plays a significant role since the six large strike-slip events occur in this region. On the other hand, the seismicity waxes and wanes over time, characteristic of a magmatic process. Toward the end of the swarm, the seismicity is correlated with seafloor volcanic structures in the southwest Endeavour region. Seismic *b* values are again greater than 1 (~1.5) consistent with volcanic processes. While diffuse, the north to south migration of seismicity is suggestive of a dike propagating south from the West Valley segment, but may also be the result of progressive cracking and faulting associated with tectonic propagation of the OSC with no magma injection occurring. Whether or not magmatism is involved in the southwest Endeavour Valley region, this explanation fits the expected tectonic evolution of the OSC with eventual decapitation of the northern Endeavour ridge axis by the West Valley segment.

[59] The February 2005 seismic sequence is associated with seismic and hydrothermal perturbations at the central Endeavour vent fields that are modest and are delayed by 2.5 days. We attribute these responses to a hydrologic pressure perturbation that diffuses in the upper crustal aquifer away from the main magma intrusion event on the north Endeavour ridge. When this pressure increase reaches the hydrothermal system it opens cracks leading to seismicity as well as an increase in hydrothermal fluids in diffuse venting systems. This effect is seen primarily at the diffuse vent fields that are more sensitive to small changes in crack geometry, while the high-temperature fields are connected to a more robust crack network.

Acknowledgments

[60] We thank J. Delaney and D. Kelley for their leadership of the program that included this experiment; D. Bowman, J. Parker, H. Patel, C. Schmidt, and student participants in a Friday Harbor Laboratories research apprenticeship and the IRIS summer internship program for assistance with the initial data analysis; and M. Tolstoy and an anonymous reviewer for reviews that improved this manuscript. The W. M. Keck Foundation supported the seismic and hydrothermal data collection and analysis with matching support from the Monterey

Bay Aquarium (for ship time and ocean bottom instruments) and the University of Washington (UW) (for ship time). The National Science Foundation (NSF) supported this research (OCE-0937285 and OCE-0937006) as well as the computational facility at the University of Oregon (EAR-0651123). Collection of the high-resolution ABE bathymetry was funded by NSF, UW, and NEPTUNE Canada. Collection of the CORK pressure data was supported by the Geological Survey of Canada and NSF (OCE-0400471). This paper is PMEL contribution 3615.

References

Amitrano, D. (2003), Brittle-ductile transition and associated seismicity: Experimental and numerical studies and relationship with the *b* value, *J. Geophys. Res.*, *108*(B1), 2044, doi:10.1029/2001JB000680.

Bohnenstiehl, D. R., R. P. Dziak, M. Tolstoy, C. G. Fox, and M. Fowler (2004), Temporal and spatial history of the 1999–2000 Endeavour segment seismic series, Juan de Fuca Ridge, *Geochem. Geophys. Geosyst.*, *5*, Q09003, doi:10.1029/2004GC000735.

Bohnenstiehl, D. R., F. Waldhauser, and M. Tolstoy (2008), Frequency-magnitude distribution of microearthquakes beneath the 9°50′N region of the East Pacific Rise, October 2003 through April 2004, *Geochem. Geophys. Geosyst.*, *9*, Q10T03, doi:10.1029/2008GC002128.

Brodsky, E. E., and S. G. Prejean (2005), New constraints on mechanisms of remotely triggered seismicity at Long Valley Caldera, *J. Geophys. Res.*, *110*, B04302, doi:10.1029/2004JB003211.

Brodsky, E. E., V. Karakostas, and H. Kanamori (2000), A new observation of dynamically triggered regional seismicity: Earthquakes in Greece following the August, 1999 Izmit, Turkey earthquake, *Geophys. Res. Lett.*, *27*, 2741–2744, doi:10.1029/2000GL011534.

Brune, J. N. (1970), Tectonic stress and the spectra of seismic shear waves from earthquakes, *J. Geophys. Res.*, *75*, 4997–5009, doi:10.1029/JB075i026p04997.

Cudrak, C., and R. Clowes (1993), Crustal structure of Endeavour Ridge Segment, Juan de Fuca Ridge, from a detailed seismic refraction survey, *J. Geophys. Res.*, *98*, 6329–6349, doi:10.1029/92JB02860.

Davis, E. E., K. Becker, T. Pettigrew, B. Carson, and R. MacDonald (1992), CORK: A hydrological seal and downhole observatory for deep-ocean boreholes, *Proc. Ocean Drill. Program Initial Rep.*, *139*, 43–53.

Davis, E. E., W. Wang, R. E. Thomson, K. Becker, and J. F. Cassidy (2001), An episode of seafloor spreading and associated plate deformation inferred from crustal fluid pressure transients, *J. Geophys. Res.*, *106*, 21,953–21,963.

Dziak, R. P., and C. G. Fox (1999), The January 1998 earthquake swarm at Axial Volcano, Juan de Fuca Ridge: Hydroacousitc evidence for seafloor volcanic activity, *Geophys. Res. Lett.*, *26*, 3429–3432, doi:10.1029/1999GL002332.

Dziak, R. P., C. G. Fox, and A. E. Schreiner (1995), The June-July 1993 seismo-acoustic event at CoAxial segment, Juan de Fuca Ridge: Evidence for a lateral dike injection, *Geophys. Res. Lett.*, *22*, 135–138, doi:10.1029/94GL01857.

Dziak, R. P., W. W. Chadwick Jr., C. G. Fox, and R. W. Embley (2003), Hydrothermal temperature changes at the southern Juan de Fuca Ridge with MW 6.2 Blanco transform earthquake, *Geology*, *31*, 119–122, doi:10.1130/0091-7613(2003)031<0119:HTCATS>2.0.CO;2.

Dziak, R., W. W. Chadwick Jr., J. P. Cowen, E. Baker, R. Embley, D. R. Bohnenstiehl, and J. A. Resing (2006), Detecting volcanic events in the northeast Pacific, *Eos Trans. AGU*, *87*(4), 37.

Dziak, R. P., D. R. Bohnenstiehl, J. P. Cowen, E. T. Baker, K. H. Rubin, J. H. Haxel, and M. J. Fowler (2007), Rapid dike emplacement leads to eruption and hydrothermal plume release during seafloor spreading events, *Geology*, *35*(7), 579–582, doi:10.1130/G23476A.1.

Einarsson, P., and B. Brandsdottir (1980), Seismological evidence for lateral magma intrusion during the July 1978 deflation of the Krafla volcano in NE Iceland, *J. Geophys.*, *47*, 160–165.

Fox, C. G., and R. P. Dziak (1998), Hydroacoustic detection of seismicity on volcanic activity on the Gorda Ridge, February–March 1996, *Deep Sea Res., Part A*, *45*, 2513–2530, doi:10.1016/S0967-0645(98)00081-2.

Frohlich, C., and S. D. Davis (1993), Teleseismic *b* values; or, much ado about 1.0, *J. Geophys. Res.*, *98*, 631–644, doi:10.1029/92JB01891.

Gutenberg, B., and C. F. Richter (1944), Frequency of earthquakes in California, *Bull. Seismol. Soc. Am.*, *34*, 185–188.

Hanks, T. C., and M. Wyss (1972), The use of body-wave spectra in the determination of seismic-source parameters, *Bull. Seismol. Soc. Am.*, *62*(2), 561–589.

Hill, D. P., et al. (1993), Seismicity remotely triggered by the magnitude 7.3 Landers, California, earthquake, *Science*, *260*, 1617–1623, doi:10.1126/science.260.5114.1617.

Inderbitzen, K. E., K. Becker, and E. Davis (2008), Seafloor uplift recorded by pressures in the CORK in Hole 857D, Middle Valley, northern Juan de Fuca ridge, *Eos Trans. AGU*, *89*(53), Fall Meet. Suppl. Abstract T23A-2007.

Johnson, H. P., M. Hutnak, R. P. Dziak, C. G. Fox, I. Urcuyo, J. P. Cowen, J. Nabalek, and C. Fisher (2000), Earthquake-induced changes in a hydrothermal system on the Juan de Fuca Ridge mid-ocean ridge, *Nature*, *407*, 174–177, doi:10.1038/35025040.

Karsten, J. L., J. R. Delaney, J. M. Rhodes, and R. A. Liias (1990), Spatial and temporal evolution of magmatic systems beneath the Endeavour segment, Juan de Fuca Ridge: Tectonic and petrologic constraints, *J. Geophys. Res.*, *95*, 19,235–19,256.

Kelley, D. S., J. A. Baross, and J. R. Delaney (2002), Volcanoes, fluids, and life at mid-ocean ridge spreading centers, *Annu. Rev. Earth Planet. Sci.*, *30*, 385–491, doi:10.1146/annurev.earth.30.091201.141331.

Kilb, D., J. Gomberg, and P. Bodin (2000), Triggering of earthquake aftershocks by dynamic stresses, *Nature*, *408*, 570–574, doi:10.1038/35046046.

Koyanagi, R. Y., W. R. Tanigawa, and J. S. Nakata (1988), Seismicity associated with the eruption, in *The Puu Oo Eruption of Kilauea Volcano, Hawaii: Episodes 1 Through 2, January 3, 1983, Through June 8, 1984*, edited by E. Wolfe, pp. 183–235, U.S. Geol. Surv., Reston, Va.

Lilley, M. D., D. A. Butterfield, J. E. Lupton, and E. J. Olson (2003), Magmatic events can produce rapid changes in hydrothermal vent chemistry, *Nature*, *422*, 878–881, doi:10.1038/nature01569.

Love, B. (2008), The origin, measurement and fate of volatiles in hydrothermal systems through plume studies, time series analysis and sensor development, Ph.D. thesis, Univ. of Wash., Seattle.

McClain, J. S., M. L. Begnaud, M. A. Wright, J. Fondrk, and G. K. Von Damm (1993), Seismicity and tremor in a submarine hydrothermal field: The northern Juan de Fuca Ridge, *Geophys. Res. Lett.*, *20*, 1883–1886, doi:10.1029/93GL01872.

Patel, H. (2007), Spatial and temporal seismicity patterns of the February/March 2005 swarm on the Endeavour Segment, Juan de Fuca Ridge, M.Sc. thesis, Univ. of Oreg., Eugene.

Pavlis, G. L., F. Vernon, D. Harvey, and D. Quinlan (2004), The generalized earthquake-location (GENLOC) package: An earthquake-location library, *Comput. Geosci.*, *30*(9–10), 1079–1091, doi:10.1016/j.cageo.2004.06.010.

Pawlowicz, R., B. Beardsley, and S. Lentz (2002), Classical tidal harmonic analysis including error estimates in MATLAB using T_TIDE, *Comput. Geosci.*, *28*, 929–937, doi:10.1016/S0098-3004(02)00013-4.

Pollard, D. D., and A. Aydin (1984), Propagation and linkage of oceanic ridge segments, *J. Geophys. Res.*, *89*(B12), 10,017–10,028.

Ristau, J., G. C. Rogers, and J. F. Cassidy (2003), Moment magnitude–local magnitude calibration for earthquakes off Canada's west coast, *Bull. Seismol. Soc. Am.*, *93*, 2296–2300, doi:10.1785/0120030035.

Rohr, K. M. M., B. Milkereit, and C. J. Yorath (1988), Asymmetric deep crustal structure across the Juan de Fuca Ridge, *Geology*, *16*, 533–537, doi:10.1130/0091-7613(1988)016<0533:ADCSAT>2.3.CO;2.

Romanowicz, B., D. Stakes, R. Uhrhammer, P. McGill, D. Neuhauser, T. Ramirez, and D. Dolenc (2003), The MOBB experiment: A prototype permanent off-shore ocean bottom broadband station, *Eos Trans. AGU*, *84*(34), 325.

Rubin, A. M., and D. Gillard (1998), Dike-induced earthquakes: Theoretical considerations, *J. Geophys. Res.*, *103*, 10,017–10,030.

Scholz, C. H. (1968), The frequency-magnitude relation of microfracturing in rock and its relation to earthquakes, *Bull. Seismol. Soc. Am.*, *58*, 399–415.

Seyfried, W. E., Jr., J. S. Seewald, M. E. Berndt, K. Ding, and D. I. Foustoukos (2003), Chemistry of hydrothermal vent fluids from the Main Endeavour Field, northern Juan de Fuca Ridge: Geochemical controls in the aftermath of June 1999 seismic events, *J. Geophys. Res.*, *108*(B9), 2429, doi:10.1029/2002JB001957.

Sohn, R. A., J. A. Hildebrand, and S. C. Webb (1999), A microearthquake survey of the high-temperature vent fields on the volcanically active East Pacific Rise, *J. Geophys. Res.*, *104*, 25,367–25,377.

Solomon, S. C., P. Y. Huang, and L. Meinke (1988), The seismic moment budget of slowly spreading ridges, *Nature*, *334*, 58–60, doi:10.1038/334058a0.

Stakes, D., J. McClain, T. VanZandt, P. McGill, and M. Begnaud (1998), Corehole seismometer development for low-noise seismic data in a long-term seafloor observatory, *Geophys. Res. Lett.*, *25*, 2745–2748, doi:10.1029/98GL01937.

Thatcher, W., and T. C. Hanks (1973), Source parameters of southern California earthquakes, *J. Geophys. Res.*, *78*(35), 8547–8576, doi:10.1029/JB078i035p08547.

Tolstoy, M. (2008), Seismological constraints on magmatic and hydrothermal processes at ridges, in *Magma to Microbe: Modeling Hydrothermal Processes at Ocean Spreading Centers*, *Geophys. Monogr. Ser.*, vol. 178, edited by R. P. Lowell et al., pp. 75–96, AGU, Washington, D. C.

Toomey, D. R., S. C. Solomon, and G. M. Purdy (1988), Microearthquakes beneath the median valley of the Mid-Atlantic Ridge near 23°N: Tomography and tectonics, *J. Geophys. Res.*, *93*, 9093–9112, doi:10.1029/JB093iB08p09093.

Tréhu, A. M., and S. C. Solomon (1983), Earthquakes in the Orozco transform zone: Seismicity, source mechanisms, and tectonics, *J. Geophys. Res.*, *88*, 8203–8225.

Utsu, T. (1961), A statistical study on the occurrence of aftershocks, *Geophys. Mag.*, *30*, 521–605.

Van Ark, E. M., R. S. Detrick, J. P. Canales, S. M. Carbotte, A. J. Harding, G. M. Kent, M. R. Nedimovic, W. S. D. Wilcock, J. B. Diebold, and J. M. Babcock (2007), Seismic structure of the Endeavour Segment, Juan de Fuca Ridge: Correlations with seismicity and hydrothermal activity, *J. Geophys. Res.*, *112*, B02401, doi:10.1029/2005JB004210.

Wiemer, S., and M. Wyss (2002), Mapping spatial variability of the frequency-magnitude distribution of earthquakes, *Adv. Geophys.*, *45*, 259–302.

Wiemer, S., S. R. McNutt, and M. Wyss (1998), Temporal and three-dimensional spatial analyses of the frequency-magnitude distribution near Long Valley Caldera, California, *Geophys. J. Int.*, *134*, 409–421, doi:10.1046/j.1365-246x.1998.00561.x.

Wilcock, W. S. D. (2004), Physical response of mid-ocean ridge hydrothermal systems to local earthquakes, *Geochem. Geophys. Geosyst.*, *5*, Q11009, doi:10.1029/2004GC000701.

Wilcock, W. S. D., and D. R. Toomey (1991), Estimating hypocentral uncertainties from marine microearthquake surveys: A comparison of generalized inverse and grid search methods, *Mar. Geophys. Res.*, *13*, 161–171.

Wilcock, W. S. D., S. D. Archer, and G. M. Purdy (2002) Microearthquakes on the Endeavour segment of the Juan de Fuca Ridge, *J. Geophys. Res.*, *107*(B12), 2336, doi:10.1029/2001JB000505.

Wilcock, W. S. D., A. H. Barclay, P. McGill, D. Stakes, T. Ramirez, D. Toomey, D. Durant, E. Hooft, T. Mulder, and J. Ristau (2004), Local earthquakes on the Endeavour segment of the Juan de Fuca Ridge: First seismic results from the Keck seismic/hydrothermal observatory, *Eos Trans. AGU*, *85*(47), Fall Meet. Suppl., Abstract B13A-0180.

Wilcock, W. S. D., E. E. E. Hooft, D. R. Toomey, P. R. McGill, A. H. Barclay, D. S. Stakes, and T. M. Ramirez (2009), The role of magma injection in localizing black smoker activity, *Nat. Geosci.*, *2*, 509–513, doi:10.1038/ngeo550.

Wyss, M., C. G. Sammis, R. M. Naudeau, and S. Wiemer (2004), Fractal dimension and b-value on creeping and locked patches of the San Andreas Fault near Parkfield, California, *Bull. Seismol. Soc. Am.*, *94*, 410–421, doi:10.1785/0120030054.